analytical chemistry

pubs.acs.org/ac Article

Optoelectronic Gas Sensor Based on Few-Layered InSe Nanosheets for NO_2 Detection with Ultrahigh Antihumidity Ability

Lu Zhang,[▽] Zhongjun Li,[▽] Jiang Liu, Zhengchun Peng, Jia Zhou,* Han Zhang,* and Yingchun Li*

Cite This: *Anal. Chem.* 2020, 92, 11277−11287 Read Online

ACCESS | Metrics & More | Article Recommendations | Supporting Information

ABSTRACT: Two-dimensional (2D) transition-metal/metal chalcogenides including MoS_2, $MoSe_2$, WS_2, SnS_2, etc. have shown considerable potential for the fabrication of gas sensors for NO_2 detection. However, these sensors usually suffer from sluggish and incomplete recovery at room temperature, and their sensitivities are limited by presorbed O_2. In this work, a novel optoelectronic gas sensor based on direct-bandgap InSe nanosheets was demonstrated. Because of the excellent photoelectric and sensing properties in few-layer InSe, detection of NO_2 at room temperature was realized. Ultrahigh and reversible responses were obtained under ultraviolet (UV) light illumination, and the limit of detection (0.98 ppb) was ~40 times lower than that observed without UV light. Furthermore, the effects of O_2 and H_2O molecules on sensor performance were fully studied through experiments and density functional theory. Some new mechanisms of NO_2 detection in high relative humidity conditions under UV illumination were proposed, including regulation of proton transfer and induction of H_2O_2 reduction. In all, this work not only broadens the application field of 2D InSe, but also demonstrates the potential prospect of detecting ppb-level NO_2 in complex circumstances such as human breath by using 2D material-based sensors with light activation.

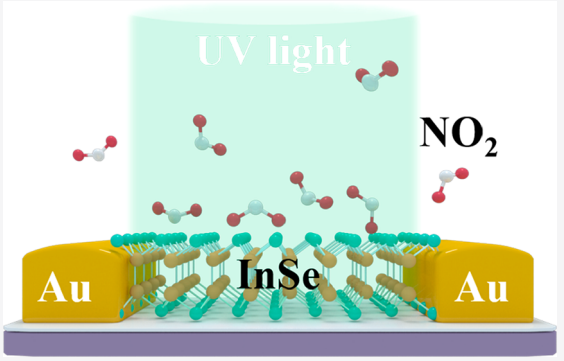

Downloaded via SHENZHEN UNIV on February 1, 2021 at 01:41:08 (UTC).
See https://pubs.acs.org/sharingguidelines for options on how to legitimately share published articles.

Nitrogen dioxide (NO_2) is one of the atmospheric pollutants released from fuel combustion and automotive engines, which can cause numerous environmental issues, such as dense fog and acid rain.[1] In addition, long-term exposure to only trace (ppb) levels of NO_2 gas can have adverse effects on human respiratory system and skin.[2,3] The concentration of NO_2, furthermore, can reflect the level of nitrogen oxides (NO_x, a species of NO, NO_2, etc.) in exhaled breath, where NO_x can be considered as a biomarker to diagnose diseases such as nasal polyposis, chronic obstructive pulmonary disease, etc.[4,5] Therefore, detection of NO_2 gas is of the great importance for protecting the environment and human beings, as well as assessing health status.

Chemiresistive gas sensors are one of the most common and effective instruments for detecting trace gas molecules.[6−8] In recent years, two-dimensional (2D) materials are gaining great attention for use in designing gas sensors, because of their excellent semiconductor properties and high surface-area-to-volume ratio.[9] Compared with conventional gas sensors based on metal oxides, 2D-material-based gas sensors can fully interact with target gas and can work in the absence of oxygen ions, resulting in decent gas-sensing performance, even at room temperature (RT).[10] 2D transition-metal dichalcogenides (TMDs) and metal chalcogenides (MCs), such as MoS_2,[11] WS_2,[12] and SnS_2,[13] have recently been verified as ideal candidates for sensing NO_2 by virtue of their high binding energy and large charge transfer number for adsorbing NO_2 molecules. Unfortunately, these sensors usually display a lengthy response to NO_2 and incomplete recovery at RT.[14] Besides, sensing behavior could be impaired by the preadsorbed oxygen species that are dwelling on the surface of sensing materials and occupying active sites.[15] For this, light irradiation has been used as an effective tactic that not only shortens response/recovery time, but also helps to release oxygen species. However, a prerequisite of this method is that the sensing materials should possess good photoelectric properties.[16,17]

Indium selenide (InSe), as a nova in the class of 2D MCs, is a van der Waals layered material with an electron effective mass of ~0.143 m_0, and band gaps of 1.26 eV for the bulk and 2.11 eV for the single-layer at RT.[18,19] InSe has been widely used to fabricate optoelectronic devices, because of their high on/off ratios (~10^8),[20] high carrier mobility (~1000 $cm^2\ V^{-1}\ s^{-1}$ at RT),[21] good stability in air (compared with phosphene), and excellent photoresponsivity with broad spectral range from UV to near-infrared.[21,22] In addition, density functional theory

Received: May 5, 2020
Accepted: July 20, 2020
Published: July 20, 2020

© 2020 American Chemical Society

https://dx.doi.org/10.1021/acs.analchem.0c01941
Anal. Chem. 2020, 92, 11277−11287

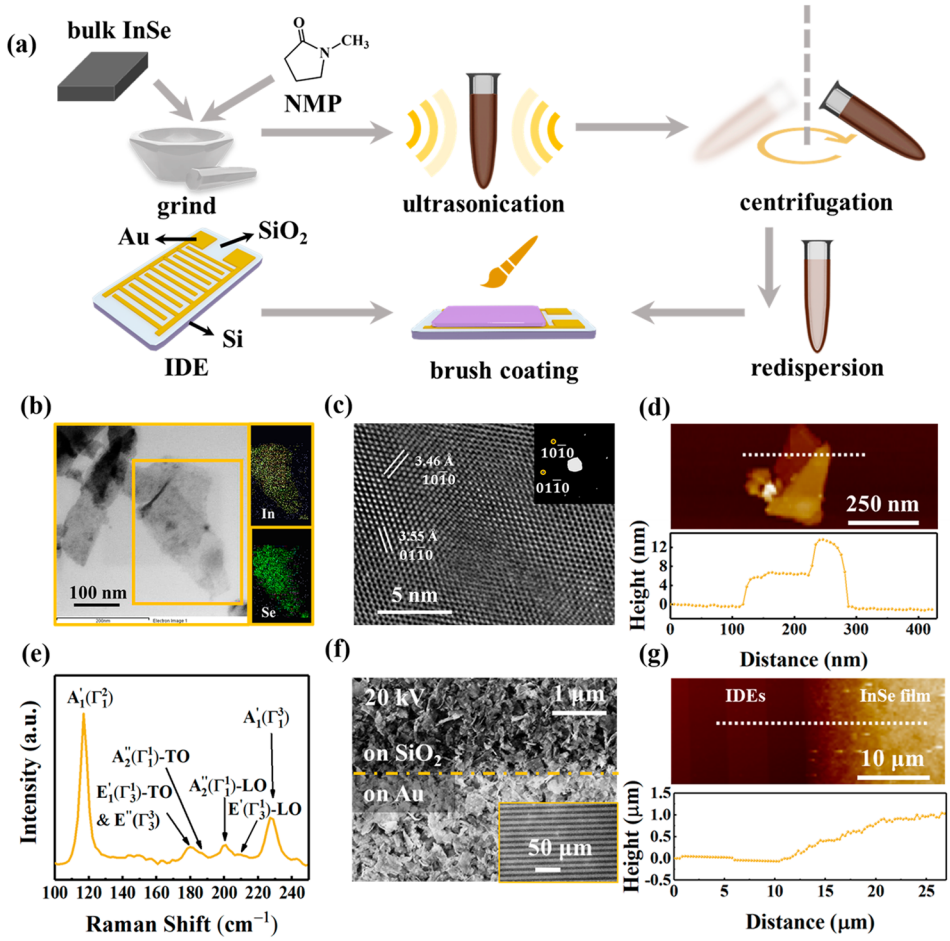

Figure 1. (a) Preparation of InSe by LPE method and fabrication of InSe/IDEs. (b) TEM and EDS mapping of prepared InSe nanosheets. (c) High-resolution transmission electron microscopy (HRTEM) image of the InSe (inset shows the selected-area electron diffraction (SAED) pattern). (d) Atomic force microscopy (AFM) of representative InSe nanosheets and height profile of the indicated section (white dashed lines). (e) Raman spectra for InSe samples on IDEs. (f) SEM image of the surface of InSe/IDEs; the inset shows an SEM image of enlarged view with SiO_2 and Au stripes. (g) AFM of the edge of InSe film on IDEs and height profile of the indicated section (white dashed lines).

(DFT) calculations have already noted that 2D InSe has a superior gas-sensing ability for detecting open-shell molecules (NO and NO_2) based on the charge-transfer mechanism.[23,24] In addition, few-layer InSe is endowed with a direct bandgap characteristic when there are more than six layers present, which is beneficial to light absorption and thus enhances the photoelectric properties.[25] The excellent photoelectric performance of randomly stacked few-layer InSe nanosheets has been confirmed in our previous work.[26] Compared with TMDs that exhibit direct-bandgap properties only in a single layer, fewer-layer InSe nanosheets are easier to prepare and have a greater possibility of mass production by using the liquid-phase exfoliation (LPE) method.[27] Besides, according to the literature, the photoelectric and gas-sensing properties of randomly stacked 2D-material nanosheets are comparable to those of their single-crystal counterpart.[28,29] Altogether, it can be concluded that few-layer InSe nanosheets has great promise to build a photoelectric gas sensor for determining NO_2.

In this work, an optoelectronic gas sensor based on few-layered InSe nanosheets was obtained, where InSe nanosheets were prepared via the LPE method. Besides, one-chip InSe devices were also fabricated by micromechanical exfoliation method for comparison. The prepared InSe nanosheets had high crystallization with favorable thickness. The adsorption behaviors of O_2, H_2O, and NO_2 on the 2D InSe monolayer was analyzed by DFT calculation. The excellent gas-sensing performance of InSe-based sensor toward ppb-levels NO_2 under UV illumination has been proven by abundant experiments. In addition, the feasibility to detect NO_2 in human breath samples by using the InSe-based sensor was verified, and a possible sensing mechanism and the effect of UV illumination were deeply discussed.

EXPERIMENTAL SECTION

Reagents and Instruments. Bulk InSe (99.9999%) was obtained from 2D Semiconductors, Inc. (Scottsdale, AZ, USA). *N*-Methyl-2-pyrrolidone (NMP, 99.5%) was purchased from Shanghai Aladdin Co. Ltd. (Shanghai, China). Methanol, ethanol, and acetone were purchased from Titan Scientific Co., Ltd. (Shanghai, China). NO_2, H_2S, and NH_3 at 1000 ppm were obtained from Dalian Haide Tech. Co., Ltd. (Dalian, China). Synthetic air as well as pure N_2 were obtained by Guangzhou Xiangyuan Gas Co., Ltd. (Guangzhou, China). All chemicals were of analytical grade and used without further purification.

Interdigital electrodes (IDEs) were obtained from Huizhou Xinwenxiong Trade Co., Ltd. (Huizhou, China). It has a monocrystalline Si substrate with 300 nm SiO_2 on the top, and Cr/Au (10 nm/100 nm) electrodes were deposited on the

https://dx.doi.org/10.1021/acs.analchem.0c01941
Anal. Chem. 2020, 92, 11277−11287

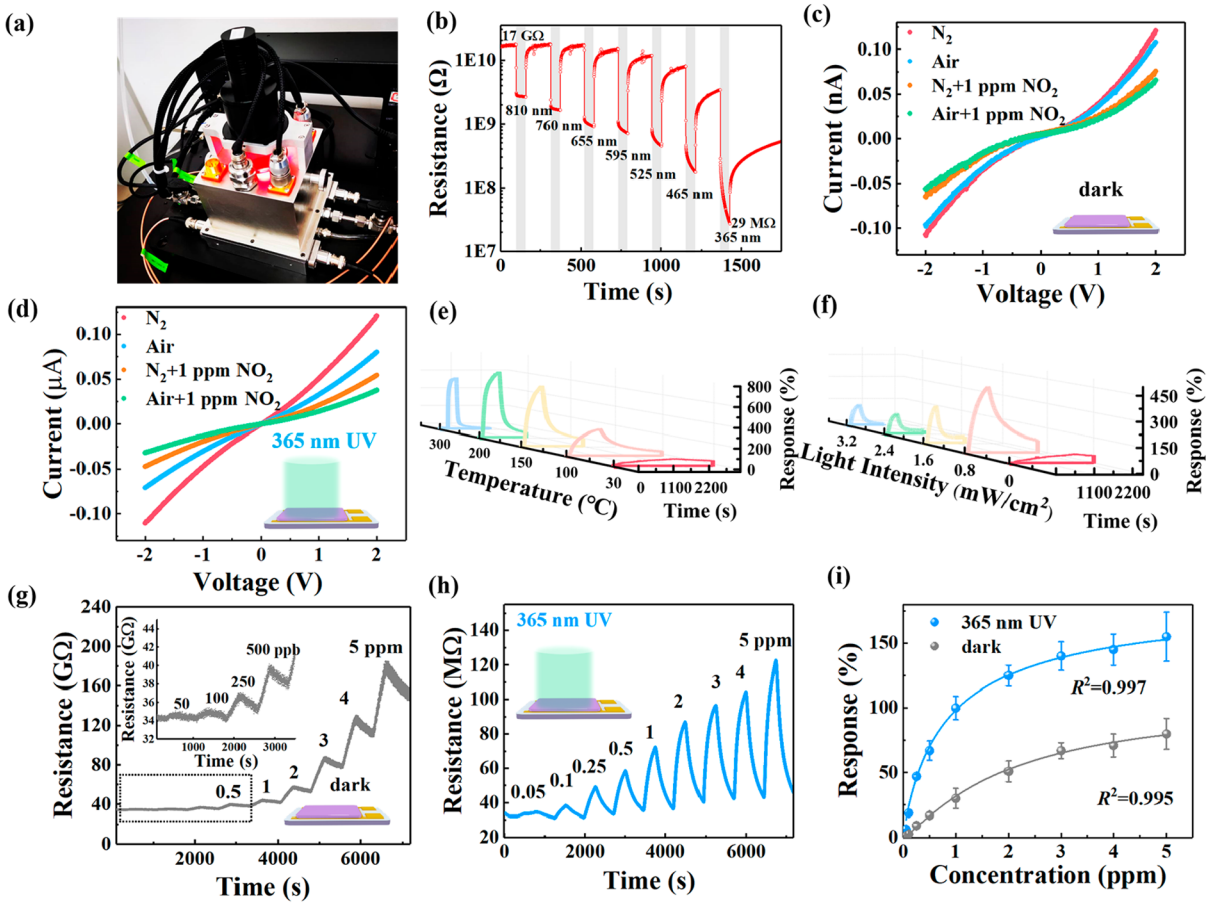

Figure 2. (a) Photograph of the gas chamber used for testing sensing performance. (b) Dynamic response curve of InSe/IDEs to irradiation of different wavelengths. *I*−*V* curves of InSe/IDEs under different gas atmospheres (c) in darkness conditions and (d) under 365-nm light. Response curves of InSe/IDEs to 1 ppm of NO_2 gas (e) at different temperatures in a dark environment and (f) under different light intensities of 365-nm UV light. Dynamic response curves of InSe/IDE for 0.05−5 ppm of NO_2 gas (g) in a dark environment and (h) under 365-nm UV light (the inset shows the amplified curve at low concentrations). (i) Response intensity curves of InSe/IDEs for 0.05−5 ppm of NO_2 (n = 3). All operating temperatures are 30 °C, with a total gas flow rate of 1000 sccm; all background gases are air, except the test of *I*−*V* curves, and all light intensities are 3.2 mW/cm^2, unless noted otherwise.

surface of SiO_2. In this experiment, the width of the Au strip and strip space is 5 μm for loading InSe-nanosheets film, and 30 μm electrode strips with 20 μm strip space were designed to fabricate the one-chip InSe device.

The morphology was characterized by using a scanning electron microscopy (SEM) system (Zeiss, Model SIGMA) that was operating at 20 kV and a high-resolution transmission electron microscopy (TEM) system (JEOL, Model JEM 2100F). The structure of the prepared InSe was investigated using a Raman microscope (Horiba LabRAM HR800) with a 532 nm laser source. The absorption spectra of InSe nanosheets was obtained using a spectrophotometer (Model UH4150, Hitachi, Tokyo, Japan). The thickness distribution of the InSe film/layer was acquired using an atomic force microscopy (AFM) system (Bruker Dimension Ico). Electrical signals of the sensors were collected using a CGS-MT Micro Analysis System (Beijing Elite Tech. Co., Ltd., Beijing, China). A dynamic gas distribution device (Model DGL-III) was also purchased from Beijing Elite Tech. Co., Ltd. (Beijing, China). Light-emitting diodes (LEDs) with different wavelengths that were used to illuminate the device were purchased from EPILEDS Tech. Co., Ltd. (Taiwan, China).

Preparation of InSe Nanosheets. InSe nanosheets were obtained through the LPE method. Briefly, 200 mg of bulk InSe crystal was added in 20 mL of NMP, and then the mixture was ground in an agate mortar for 60 min, followed by further ultrasonication for 8 h at a power of 300 W at temperatures of <20 °C (to decrease possible degradation at elevated temperature). Subsequently, the obtained liquid was centrifuged at a speed of 2500 rpm for 5 min. The supernatant was sucked out and further centrifuged at 18 000 rpm for 10 min; the final sediment was collected and redispersed in 5 mL of NMP.

Preparation of InSe Gas Sensors. First, the IDEs were soaked in acetone for 15 min, followed by washing with ethanol and deionized water successively, and drying with nitrogen at 50 °C. After that, InSe nanosheets (3.2 mg/mL) were painted on the surface of IDEs by using ultrafine brush. Compared with spin coating and screen-printing methods, brush coating has minimum requirements toward the coating material, the coated substrate and the equipment. In addition, it is relatively easy to control the modified area compared with drop coating. The prepared sensors (InSe/IDEs) were then dried in a vacuum oven at 90 °C for 2 h.

For comparison, one-chip InSe sensors were prepared by a micromechanical exfoliation method using a hand-built 2D-material transfer platform.

https://dx.doi.org/10.1021/acs.analchem.0c01941
Anal. Chem. 2020, 92, 11277−11287

Gas-Sensing Experiments. The gas sensing performances of InSe/IDEs were investigated through a commercial gas-sensing measurement system. An InSe/IDEs was placed into a mini probe station consisting of a stainless-steel chamber with the size of 1 L and a source and measurement meter. A certain amount of target gases with a dynamic humidity were independently injected into the chamber, which were controlled by a gas distribution device. The device contains 5 mass flow controllers and a humidity control unit, whose schematic diagram can be seen in Figure S1 in the Supporting Information. All the measurements were performed at a bias voltage of 1 V at RT. The total gas flow rate was fixed at 1000 sccm, and the diluting gas (background gas) was N_2 or dry air. Sensor response is defined (expressed as a percentage) as $((R_g - R_0)/R_0) \times 100$, where R_g and R_0 is sensor resistance when exposed to gas analyte or background gas, respectively. Herein, the response/recovery time is set as the time to reach 90% response/recovery equilibrium upon exposure to target gas or background gas.

Prior to use, the devices were stabilized under UV irradiation in N_2 for 30 min.

RESULTS AND DISCUSSION

Characterizations of Materials and Devices. InSe nanosheets were obtained via the LPE method, and the preparation process is briefly described in Figure 1a. TEM analysis was performed to investigate the morphology of the as-prepared InSe nanosheets. As shown in Figure 1b, the nanosheets have intact nanoscale structure with wide lateral dimensions (~200 nm). Energy-dispersive X-ray spectroscopy (EDS) mapping of selective area (Figure 1b) reflects that In and Se elements are uniformly distributed over a piece of sheet, and their atomic ratio is ~1:1, according to the EDS spectra (see Figure S2a in the Supporting Information). Clear lattice fringes in the HRTEM image in Figure 1c suggest high crystallinity of the nanosheets. An interplanar spacing of 3.46 or 3.55 Å corresponds to lattice surface $(10\bar{1}0)$ or $(01\bar{1}0)$ of pristine InSe (JCPDS File No. 34-1431). SAED pattern (insert of Figure 1c) taken from the HRTEM image exhibits clear diffraction spots, which can be also matched with the structural information on pristine InSe crystal. AFM image (Figure 1d) shows typical InSe nanosheets on silicon wafer, and average thickness value is 5.75 ± 0.20 nm (n = 40). The thickness distribution of InSe can be seen in Figures S2b and S2c in the Supporting Information. According to the previous reports, the interlayer distance of InSe nanosheets is ~0.83 nm,[30,31] indicating that most of InSe nanosheets have a seven-layer structure. Besides, InSe can change from indirect bandgap to direct bandgap as the number of layers increases up to six. Thus, it is reasonable to deduce that the as-prepared InSe nanosheets have a direct bandgap, which is favorable for the generation of photogenerated carriers.[25] Since the productivity of nanosheets by LPE method has a positive correlation with the thickness within a certain range, fewer layers of InSe nanosheets are easier to prepare, in comparison with TMDs that only exhibit direct band gaps in a monolayer. Figure 1e exhibits the Raman spectrum of InSe on IDEs. Seven characteristic modes of InSe can be observed at 532 nm laser excitation. $A_1'(\Gamma_1^2)$ at 117 cm^{-1}, $E_1'(\Gamma_3^1)$-TO'' and $E''(\Gamma_3^3)$ at 179 cm^{-1}, $A_2''(\Gamma_1^1)$ at 200 cm^{-1} and $A_1''(\Gamma_1^3)$ at 227 cm^{-1} can be accredited to the modes of bulk InSe. In addition, the presence of $A_2''(\Gamma_1^1)$ at 187 cm^{-1} and $E''(\Gamma_1^3)$-LO at 211 cm^{-1} implies that most InSe are few-layer nanosheets.[31] The morphology of InSe/IDE in the SEM image (Figure 1f) shows that the InSe nanosheets are randomly and uniformly distributed on the electrode surface. Importantly, the resulting InSe membrane is fluffy and porous, which is beneficial to molecular and Knudsen diffusion. The high-resolution SEM image of InSe film can be seen in Figure S2d in the Supporting Information. The AFM graph (Figure 1g) illustrates that the thickness of InSe film on IDE is ~1 μm. The related characterizations of the one-chip InSe device are shown in Figure S3 in the Supporting Information.

Electrical Characteristics and Gas-Sensing Performance of the Sensors. All the prepared devices were tested in a small probe station (gas chamber), as displayed in Figure 2a, where parallel light rays can enter from the quartz glass above the chamber and illuminate all of the sensors vertically. First, the photoresponse intensity of InSe/IDEs was investigated. As shown in Figure 2b, InSe/IDEs demonstrated a broad photoresponse to the radiation from UV to near-infrared (NIR). The resistance of InSe/IDEs decreased as the wavelength decreased, which is in good agreement with previous reports.[19,32] The resistance especially decreased by 3 orders of magnitude in the case of UV irradiation (from ~17 GΩ to ~29 MΩ), which might be attributed to multiple exciton generation.[33] Some details of the multiple exciton generation are described in Figure S4 in the Supporting Information. In this experiment, an excitation wavelength of 365 nm was used to study gas-sensing characteristics, since more photogenerated electrons can be generated under 365-nm irradiation than under visible light. Note that the photoresponse/decay time is relatively slow, compared with reported 2D-material-based photodetectors, which may be related to interface defects, dangling bonds, and oxygen adsorbed on the surface of InSe nanosheets.[34,35] Apart from photoresponse, stability and repeatability of InSe/IDEs toward 365-nm irradiation were also tested, and the results are given in Figure S5 in the Supporting Information.

The $I-V$ characteristics of InSe/IDEs were studied as displayed in Figures 2c and 2d. Consistent with the above results, the current values were increased by 3 orders of magnitude with the illumination of UV light. Besides, it is noticed that there is an obvious nonlinear relationship between current and voltage, indicating the existence of Schottky contact between the InSe nanosheets and the Au electrode.[36] According to previous studies, the Schottky contact device might possess higher sensitivity to the target gas, compared with an ohmic contact device.[37] In addition, the currents of the device under nitrogen and air atmospheres were different. This is because O_2 molecules in air can capture electrons on the InSe surface, resulting in a decrease in current. When the sensor was exposed to NO_2, which is a strong electron acceptor, the current further decreased significantly. These results prove the possibility of the sensor to detect NO_2 both in nitrogen and air atmospheres.

Figure 2e presents the responses of InSe/IDEs toward 1 ppm of NO_2 at different operating temperatures, ranging from 30 °C to 300 °C. In this experiment, the sensor was first exposed to NO_2 with a concentration of 1 ppm. Air was injected into the gas chamber to replace the target gas when the resistance became stable. It can be observed that the sensing response increased gradually with temperature until 200 °C (from 35% to 688%) and decreased with further temperature elevation. Such a phenomenon is similar to the trend of traditional NO_2 sensors, based on metal oxide.[38,39]

https://dx.doi.org/10.1021/acs.analchem.0c01941
Anal. Chem. 2020, 92, 11277−11287

Table 1. 2D-Material-Based Gas Sensors for Detecting NO_2

sensing material	detection range (ppm)	response (ppm^{-1})	working state	response/recovery times (s)	ref
p-type graphene layers	1−10	12%	100 °C, air	1000/>3600	42
n-type SnS_2 flaks	0.6−10	360%	120 °C, air	170/140	43
p-type $PtSe_2$ layers	0.1−1	0.25%	RT, N_2	30/10	44
p-type $MoSe_2$ nanosheets	5−100	3%	RT, N_2	300/600	29
p-type $MnPS_3$ nanosheets	0.1−80	400%	RT, N_2	96/220	45
p-type NbS_2 nanosheets	0.5−10	3%	RT, air	3000/9000	46
p-type SnS flakes	0.15−3.75	18%	60 °C and 0.3 mW/cm^2, white light, air	40/1040	47
n-type SnS_2/rGO hybrids	0.125−1	650%	1 mW/cm^2, red light, air	75/242	48
p-type $MoTe_2$ layers	0.5−100	900%	2.5 mW/cm^2, UV, N_2	300/120	41
n-type MoS_2 nanosheets	5−100	3.6%	1.2 mW/cm^2, UV, Ar	29/350	36
n-type InSe nanosheets	0.05−5	190%	3.2 mW/cm^2, UV, air	233/350	this work
		402%	0.8 mW/cm^2, UV, air	470/1400	this work

Briefly, when a sensor works at low temperature, electrons are insufficient for adequate adsorption of NO_2 in the environment, leading to low sensing response. As the temperature increases, increases in the thermal energy generates more thermally excited electrons, thereby enhancing the sensitivity. However, with further increases in temperature, the accelerated desorption of molecules becomes the dominant factor, which weakens the interaction between NO_2 and InSe nanosheets. In this stage, the response is restrained by quick desorption of NO_2. Apart from response intensity, temperature also has a large effect on response/recovery time. The reduction of response/recovery time with increases in temperature is shown in Figure 2e, and the resistance can be fully restored to the initial state after re-exposure in air under high temperature. Note that the prepared device can still maintain a good response to NO_2 with temperatures increasing up to 300 °C. The good stability in air at high temperature may be due to the formation of a dense oxide layer on the surface of InSe, where the sensing principle might be based on the interaction between In_2O_3 and NO_2. The response data and the relative recovery rate under different temperatures can be clearly seen in Table S1 in the Supporting Information.

The above results suggest that increasing the temperature could significantly boost sensor performance. However, long-term work at high temperature causes high energy consumption and safety issues. At this point, light irradiation, as an alternative method, can play an important role in enhancing sensing behavior. Some literature has that light illumination could reduce the binding energy of materials toward gas molecules, which can further shorten response/recovery time, compared with the heating method.[40] Figure 2f displays the responses of InSe/IDEs toward 1 ppm of NO_2 at different UV intensities in the range of 0−3.2 mW/cm^2. Similar to that observed with increasing temperature, illumination can significantly improve the sensing ability for NO_2. When the power was set at 0.8 mW/cm^2, the sensing performance could compare favorably with that at 150 °C. In addition, one can observe that response as well as response/recovery time decreased and recovery rate increased with increases in light intensity. This phenomenon could be explained as described below. A certain intensity of UV illumination can produce sufficient photogenerated electron−hole pairs. The photogenerated electrons could induce adsorption of NO_2 and elevate sensing response. Besides, the reaction of photogenerated holes with negatively charged NO_2 promotes desorption of NO_2. However, further increased light intensity results in high-speed desorption of NO_2, which accelerates recovery but weakens sensing response.[41] Response and recovery rate under different light intensities are presented in Table S1. Herein, a working intensity of 3.2 mW/cm^2 was chosen in further investigations, since a rapid and recoverable response is essential in practical applications. Figures 2g and 2h present the dynamic response curves of InSe/IDEs for 0.05−5 ppm of NO_2 gas in a dark environment and under 365-nm UV irradiation, where responses had a positive correlation with NO_2 concentrations. It can be seen that the device recoveries are slow and incomplete under darkness conditions, which could be due to the high binding energy of InSe toward NO_2. In comparison, under UV irradiation, the recovery speed is greatly improved. Also, the lower noise level of the sensor under light irradiation, in comparison with that observed under darkness conditions, is another advantage of the sensor.

Figure 2i shows the corresponding relationship between sensor response and NO_2 concentration. The as-prepared device under UV excitation exhibited an ∼3 times higher response than that observed under darkness conditions. The data points fit well with the Langmuir isotherm. The equations are

$$\text{response}\ (\%) = \frac{209.23}{(1/C_{0.88}) + 1.12} \qquad \text{(under UV conditions)}$$

and

$$\text{response}\ (\%) = \frac{44.52}{(1/C_{1.20}) + 0.43} \qquad \text{(under darkness conditions)}$$

where C is the concentration of NO_2 (with units of ppm). The limit of detection (LOD) under 365-nm irradiation is estimated to be 0.98 ppb (signal-to-noise ratio (S/N) = 3), which is 40 times lower than that under darkness conditions (∼40 ppb). The performances of some recent NO_2 sensors based on 2D material are summarized in Table 1. It can be observed that the UV-illuminated InSe/IDEs exhibits a decent response for trace NO_2 with an acceptable response/recovery time, even under an air environment. Note that materials with *p*-type features have higher sensitivity to oxidizing gases (such as NO_2).[41] Further improvement in sensing NO_2 is expected when InSe is converted from *n*-type to *p*-type by ingenious methods. More-extensive comparison with other recently reported NO_2 sensors can be seen in Table S2 in the Supporting Information.

The performance of the one-chip InSe device was also tested (see Figure S6 in the Supporting Information). Compared with InSe nanosheets, the one-chip InSe showed responses similar to those of NO_2 with shorter response/recovery time (∼310 s/

https://dx.doi.org/10.1021/acs.analchem.0c01941
Anal. Chem. 2020, 92, 11277−11287

~300 s) under darkness conditions. However, under UV illumination (0.8 mW/cm^2), the sensor showed depressed responses, compared with that under dark conditions. This phenomenon can be attributed to the compact structure of a single chip of InSe. Gas molecules have difficulty in diffusing into the interior of the chip. Thus, the diffusion effect is negligible, while the desorption effect is more likely to occupy a dominant role under UV light illumination, so that the response is decreased. In addition, the poor stability of the one-chip device is another drawback. In our test, only ~60% response was retained after 15 days of testing.

Oxygen is one of the composition gases of air. The theoretical calculation results show that the interaction between O_2 and the InSe surface is very weak, belonging to physisorption. Figure 3a presents the most stable configuration

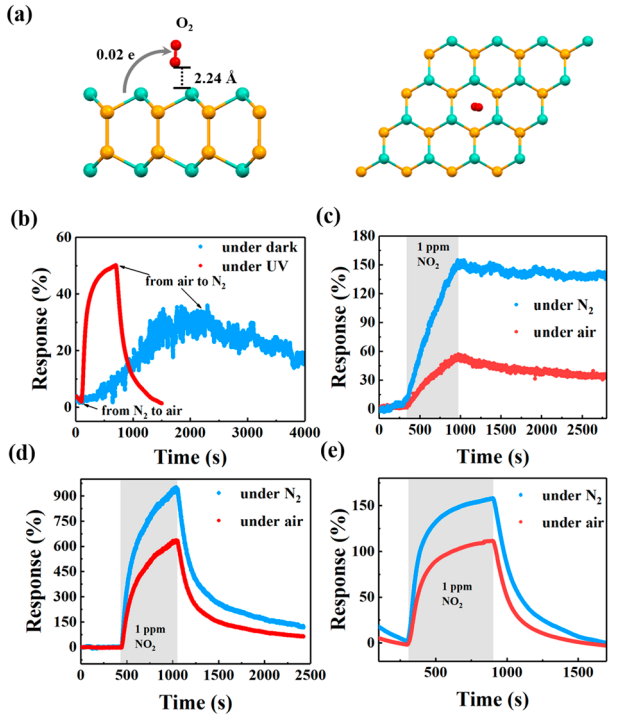

Figure 3. (a) Top and side views of the most stable configuration of O_2 on InSe, where In and Se are illustrated by orange and green balls, respectively. (b) Dynamic response of InSe/IDEs to air (210 000 ppm of O_2) and N_2 at 365 nm UV and under darkness conditions. Dynamic response of InSe/IDEs to 1 ppm of NO_2 (c) at RT and (d) at 150 °C under different vapor atmospheres. (e) Dynamic response of InSe/IDEs to 1 ppm of NO_2 under different vapor atmospheres at 365 nm UV.

of O_2 on InSe, where O_2 is almost vertical above the hexagon center, with the vertical distance of 2.24 Å. InSe has a weaker adsorption energy (−76 meV) for O_2 adsorption, in comparison with phosphene (−270 meV),[49] indicating the difficulty in oxidation of InSe under dry air conditions. As depicted in Figure 3b, the response was unrecoverable after the background was switched from air to N_2, implying the hardness of O_2 desorption from the surface of InSe without extra energy. Besides, under darkness conditions, exposure to air (containing ~21% O_2) only yielded ~30% response. The low sensitivity is consistent with the results of theoretical calculations (low charge transfer number). In comparison, with the help of UV illumination, the sensing response to O_2 was enhanced to ~50%; a much faster responding speed was obtained and the device fully recovered to its initial resistance when air was replaced with N_2. The related equations are shown below:

$$h\nu \leftrightarrow h^+_{(h\nu)} + e^-_{(h\nu)} \quad (1)$$

$$O_{2(gas)} \leftrightarrow O_{2(ads)} \quad (2)$$

$$O_{2(ads)} + e^-_{(h\nu)} \leftrightarrow O_2{}^-_{(ads)} \quad (3)$$

$$O_{2^-(ads)} + h^+_{(h\nu)} \leftrightarrow O_{2(gas)} \quad (4)$$

Similar to the effect toward NO_2, photogenerated electrons could induce the adsorption of O_2 molecules, and photogenerated holes could react with adsorbed O_2^-, which could increase the desorption of O_2. The effect of background gas on NO_2 sensing performance is revealed in Figures 3c–e. It can be seen that the presence of O_2 attenuated the sensing response to NO_2 under darkness conditions at RT. This phenomenon can be attributed to the fact that O_2 can also be considered as an electron acceptor and compete with NO_2 for combining electrons on InSe. In addition, when the working state was set at RT, the preadsorbed O_2 is stable on the surface of InSe, resulting in a limited number of free electrons (a high depletion region in InSe) and a higher energy level of surface state, compared with the Fermi level. These elements might hinder NO_2 from further adsorption on InSe. When the temperature increased to 150 °C, the oxygen species, most of which are O_2^- at this temperature,[50] could absorb thermal energy and began to desorb. Under these conditions, NO_2 molecules compete and interact with oxygen species on the InSe surface. According to previous reports, the possible reactions are as follows:[51]

$$NO_{2(gas)} \leftrightarrow NO_{2(ads)} \quad (5)$$

$$NO_{2(ads)} + e^- \leftrightarrow NO_2{}^-_{(ads)} \quad (6)$$

$$NO_{2(gas)} + O_2{}^-_{(ads)} + 2e^- \leftrightarrow NO_2{}^-_{(ads)} + 2O^-_{(ads)} \quad (7)$$

Experimental results showed that the response in air was slightly lower than that in N_2, implying that eqs 5 and 6 are dominant reactions under this circumstance. In other words, the presence of O_2 hinders the sensing response to NO_2, rather than helping NO_2 to further capture the electrons from the conduction band of InSe. The similar phenomenon can also be observed under UV irradiation, as displayed in Figure 3e. The above analyses suggest that the influence of oxygen is negligible in measuring NO_2 under UV irradiation.[52]

Humidity is another factor that must be considered, especially in exhaled gas detection. Similar to O_2, H_2O molecule can be physically adsorbed on InSe, and their most stable configuration is displayed in Figure 4a. H_2O molecule is located above the hexagon center (2.32 Å), where H atoms point to the top Se atoms. The calculated adsorption energy is −189 meV, and the number of charge transfer is around 0.08 e from InSe to H_2O. Figure 4b presents the sensing response to RH from 4% to 90% at dark condition. It can be seen that with the continuous increase of RH, the value of the response negatively increased (the resistance was decreased), indicating that water molecules seem to play a traditional n-type doping effect (as electron donor) in this process. This effect is contrary to theoretical calculations and might be explained by the proton transfer mechanism (Figure 4c).[53] When the sensor

https://dx.doi.org/10.1021/acs.analchem.0c01941
Anal. Chem. 2020, 92, 11277−11287

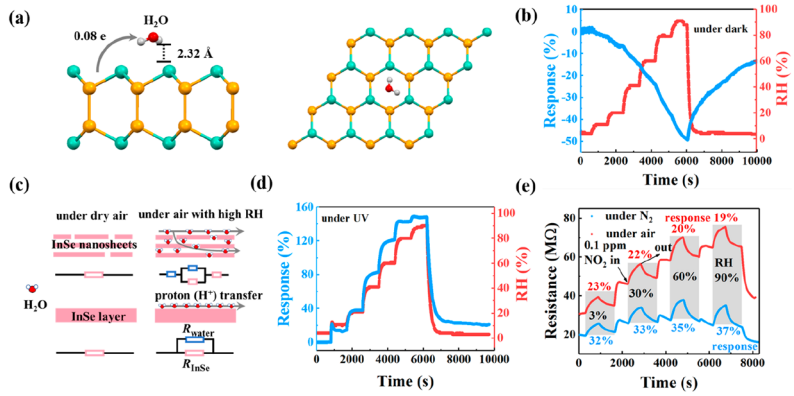

Figure 4. (a) The top and side views of the most stable configuration of H_2O on InSe. (b) Dynamic response of InSe/IDEs to different humidity under darkness conditions, where the background is air. (c) The scheme of InSe nanosheets and one-chip InSe layer and the related equivalent circuit diagram under dry air and under air with high RH. (d) Dynamic response of InSe/IDEs to different humidity levels under 365-nm UV irradiation. (e) Dynamic response of InSe/IDEs to 0.1 ppm of NO_2 at different humidity levels under 365-nm UV irradiation.

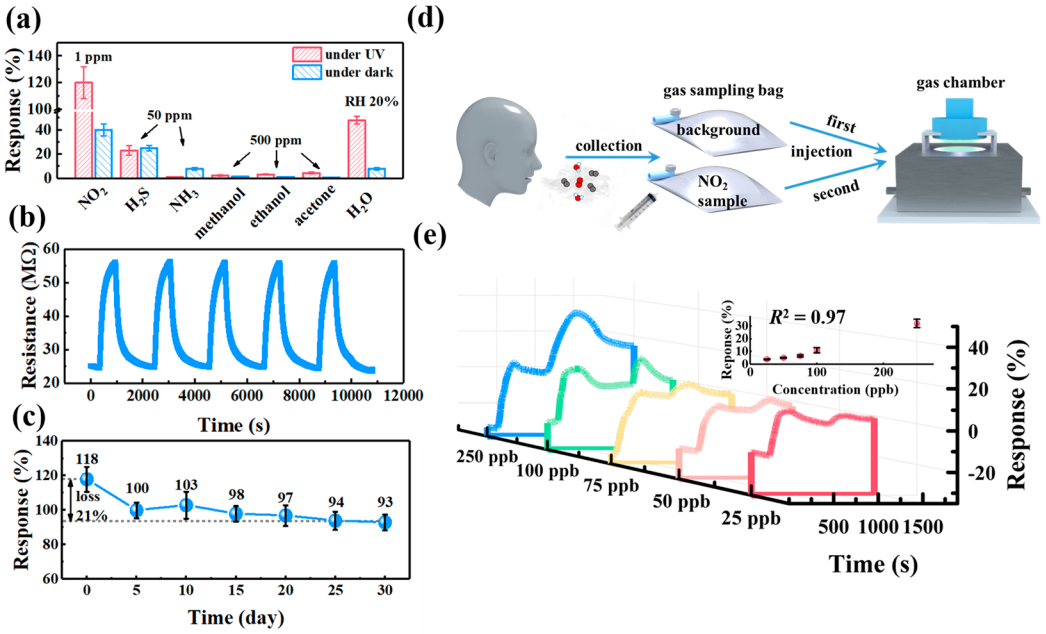

Figure 5. (a) Responses of InSe/IDEs to 1 ppm of NO_2 gas and six other gases, where the response is taken as an absolute value (n = 3). (b) Repeated dynamic responses of InSe/IDEs for 1 ppm of NO_2. (c) Long-term stability of InSe/IDEs to 1 ppm of NO_2 (n = 3). (d) Schematic process regarding breath analysis using an InSe-based sensor. (e) Response curves of InSe/IDEs to simulated NO_2 breath samples at different concentrations; inset shows calibration curves correlating the response with the concentration of NO_2 (n = 3).

was placed in dry air, the resistance mainly depends on the conductive behavior of InSe and the contact barrier. With increasing humidity, physically adsorbed H_2O molecules would aggregate on InSe to form a proton transfer layer, and H_3O^+ or H^+ would be transferred between the surface water droplets, thus reducing the resistance of the sensor. The related reaction equations are

$$H_2O_{(ads)} \leftrightarrow H^+ + OH^- \quad (8)$$

$$2H_2O_{(ads)} \leftrightarrow H_3O^+ + OH^- \quad (9)$$

Similar experimental results were obtained when the background vapor was N_2 (see Figure S7a in the Supporting Information). In addition, one-chip InSe was also tested under the same condition, and the results were shown in Figure S7b in the Supporting Information. When RH was below 60%, the device demonstrated a positive response (resistance increased). At this time, the role of H_2O in capturing electrons was mainly exhibited. When humidity continued to rise, the surface of InSe was mostly occupied by water. Proton transfer effect was dominant, and the device exhibited a negative response. Compared with a one-chip InSe layer, the InSe film stacked with nanosheets has porous structure. H_2O molecules could be more likely to diffuse into the film, so that proton-transfer effect is dominant on the change of resistance.

Interestingly, InSe/IDEs displayed different response to humidity under UV illumination (see Figure 4d, as well as Figure S7c in the Supporting Information); similar results have been reported in humidity sensors based on metal oxides.[54] Apart from direct electron capture by H_2O molecules, the increased resistance might also be contributed by the following reactions:[55]

https://dx.doi.org/10.1021/acs.analchem.0c01941
Anal. Chem. 2020, 92, 11277−11287

$$h^{+}_{(h\nu)} + H_2O_{(ads)} \leftrightarrow H^{+} + \bullet OH \quad (10)$$

$$h^{+}_{(h\nu)} + OH^{-} \leftrightarrow \bullet OH \quad (11)$$

$$2h^{+}_{(h\nu)} + 2H_2O_{(ads)} \leftrightarrow 2H^{+} + H_2O_2 \quad (12)$$

$$H_2O_2 + e^{-}_{(h\nu)} \leftrightarrow \bullet OH + OH^{-} \quad (13)$$

H_2O molecules could react with photogenerated holes and electrons, while the mobility of the electrons (~1000 $cm^2 V^{-1} s^{-1}$) was much larger than that of holes (~40 $cm^2 V^{-1} s^{-1}$) at RT, which caused an increase in InSe resistance under low RH. However, as RH continued to rise (~80%), proton transfer effect was remarkably enhanced, and thus the resistance began to show a downward trend at N_2 atmosphere. This phenomenon was not obvious in air, because more oxygen species were generated under the light excitation, which could compete with H_2O for adsorption on InSe. Briefly, O_2 might hinder the formation of H_2O membrane and weaken the proton transfer effect.

The effect of humidity on NO_2 sensing under UV irradiation is reflected in Figure 4e. In this experiment, NO_2 was injected into the gas chamber when the resistance stabilized at different RH. One can see that the sensor maintained a relatively stable response (~21% for 0.1 ppm of NO_2 in air with a relative standard deviation (RSD) of 8.69%) with increasing RH from 3% to 90%. The similar result was found under darkness conditions (Figure S7d in the Supporting Information) and for sensing 1 ppm of NO_2 (Figure S8 in the Supporting Information). The presence of H_2O seems to have no significant effect on the response toward NO_2, which has been also reported in other TMD-based gas sensors. The sensing behavior for NO_2 was relatively complicated, because there were diverse oxygen species and water derivatives existing on the interface. Besides capturing electrons directly on the InSe surface, the obtained NO_2^- might further react with H^+, which not only attenuates the proton transfer effect, but also accelerates H_2O_2 to capture electrons on InSe. The related reactions are shown in eqs 14 and 15:[53,56]

$$OH^{-}_{(ads)} + H^{+}_{(ads)} + NO_{2(gas)} + e^{-} \leftrightarrow NO_2^{-}{}_{(ads)} + H_2O_{(gas)} \quad (14)$$

$$NO_2^{-}{}_{(ads)} + H^{+} \leftrightarrow HNO_2 \quad (15)$$

Selectivity toward NO_2 against other common biomarkers in breathing gas was examined. As presented in Figure 5a, the sensor exhibited good selectivity for NO_2, under both dark and light conditions, because of the high binding energy and charge transfer of InSe for the NO_2 molecule. The related dynamic responses of InSe/IDEs for others gases are displayed in Figure S9 in the Supporting Information. To investigate repeatability, the sensor was exposed to 1 ppm of NO_2 for five cycles (Figure 5b). Clearly, a stable and recoverable response was obtained, demonstrating decent repeatability of the fabricated sensor. After testing, the devices were stored under dark air condition. Compared with the initial response, ~80% of response intensity was retained after one month, implying acceptable stability of long-term utilization (Figure 5c). Note that the surface of InSe was oxidized after a long period of use, and the gas-sensitive interface might become an $n-n$ type $InSe/In_2O_3$ heterojunction. The EDS-mapping images demonstrate the oxidation of InSe on IDEs after long-term use (see Figure S10 in the Supporting Information). Apart from that, a mild oxygen plasma treatment was used to improve the stability of sensor. The result is shown in Figure S11 in the Supporting Information.

Practicability of the sensor was investigated by analyzing simulated NO_2 breath samples. In fact, direct detection of trace NO_2 in breath samples is difficult, because of high humidity and the presence of volatile organic compounds (VOCs), which could mask sensing signals from NO_2. Herein, a blank breath sample was used as a background atmosphere. The sample containing NO_2 was injected into a gas chamber when the resistance was stabilized in a blank background. The operation process is illustrated in Figures 5d and 5e. It was found that, when the blank background was injected in, the resistance initially increased and then decreased to a stable level, which has much to do with the change in RH (from ~30% to ~85%).[57] After NO_2 samples were injected, the response had a decent positive linear relationship with the concentration of NO_2, implying good practicability in detecting ppb-level nitrogen oxides (NO_x) in exhaled gas for disease diagnosis. In real applications, the dead space gas, an exhaled gas without NO_2 molecules, could be collected and injected as the background gas.

Gas Sensing Mechanism. The gas sensing mechanism of InSe/IDEs can be attributed to the charge carrier transfer and Schottky barrier modulation, which was the same as other reported 2D-material gas sensors.[58] According to the DFT calculation, the NO_2 molecule is located ~2.69 Å above the hexagon center, and the plane of NO_2 is almost perpendicular to InSe (see Figure 6a). The binding energy and the amount of charge transfer are calculated to be −272 meV and −0.12 e, respectively, which are larger than that of other gas molecules and might be related to the coexistence of a large dipole moment of NO_2 and resonant molecular levels with the InSe states.[23] The results implied that InSe can easily and selectively adsorb NO_2 molecules, thus bringing about a big change in the number of carriers, which is comparable to the calculated results of MoS_2 (see Table 2). Although the binding energy of InSe for NO_2 is lower than that of phosphene, they show the same amount of electron transfer, which means that InSe not only possesses high sensitivity to NO_2, but also has a faster desorption rate than phosphene. As an n-type semiconductor, when InSe was exposed to NO_2 (oxidizing gas), a certain number of electrons flowed from the InSe conduction band to the adsorbed NO_2, leading to a shift of the Fermi level toward the valence band. As a result, the Schottky barrier (V_s) was enhanced and the built-in potential was decreased. In other words, the resistance of the device was increased after adsorbing NO_2, which can be illustrated by the following equation, which is suitable for n-type semiconductors.[59]

$$R = R_0 \exp\left(\frac{qV_s}{kT}\right) \quad (16)$$

Herein, R and R_0 represent the sensor resistance before and after contacting with target gas, respectively; q is the elementary charge.

V_s is the Schottky barrier from the Au/InSe and InSe/InSe interfaces, k the Boltzmann constant, and T the working temperature. In addition, the sensing film consists of randomly connected InSe nanosheets, which possess more edge sites, compared to the one-chip InSe. These sites might serve as active sites and participate in adsorption of NO_2. Besides, the actual concentration (C_I) of the target gas in the sensing film is

https://dx.doi.org/10.1021/acs.analchem.0c01941
Anal. Chem. 2020, 92, 11277−11287

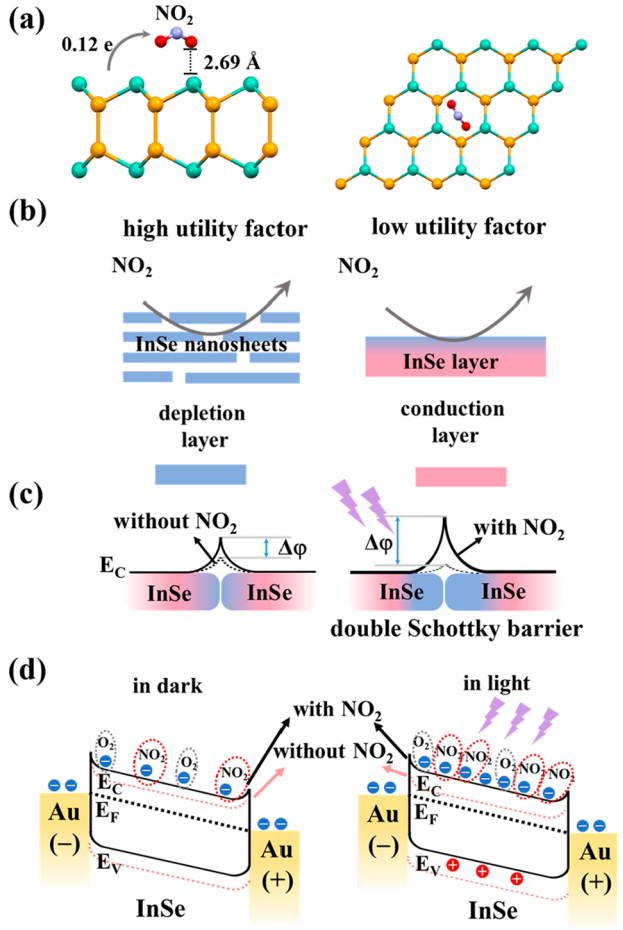

Figure 6. (a) Top and side views of the most stable configuration of NO_2 on InSe. (b) Diffusion model of NO_2 molecules at InSe-nanosheet film and at the one-chip InSe layer. (c) Potential barrier model of the InSe interface under darkness conditions and under 365 nm UV irradiation. (d) Band diagram of the sensor depicting interaction between InSe and NO_2 molecules under two conditions.

Table 2. DFT-Calculated Adsorption Energy (E_{ads}) and Charge Transfer (Q) from the Monolayer to the Adsorbed Molecule

material	molecule	E_{ads} (meV)	Q (e)	ref
InSe	O_2	−76	−0.02	this work
InSe	H_2O	−189	−0.08	this work
InSe	NO_2	−272	−0.12	this work
graphene	NO_2	−67	−0.10	60
MoS_2	NO_2	−276	−0.10	61
SnS_2	NO_2	−150	−0.05	43
phosphene	NO_2	−680	−0.12	49

less than that outside the sensing film (C_O), where the relationship between them can be probably expressed by the following equations:[62]

$$C_I = C_O \frac{\cosh\left(1\frac{x}{L}\right)L\sqrt{\frac{k}{D_k}}}{\cosh\left(L\sqrt{\frac{k}{D_k}}\right)} \quad (17)$$

$$D_K = \frac{4r}{3}\sqrt{\frac{2RT}{\pi M}} \quad (18)$$

Here, x is the depth of gas diffusion into the sensing film, L is the film thickness, D_K is the Knudsen diffusion coefficient, k is the surface reaction rate, T is the temperature, r is the pore radius of the sensing film, R is the gas constant, and M is the molecular mass of target gas. Stacked films have more molecular diffusion channels (large average pore radius), which means that InSe/IDEs has a higher "utility factor" than that of the one-chip InSe device that suffers from a high gas-dilution effect (Figure 6b).[63] Apart from that, electron capture effect of InSe/SiO_2 interface might negatively affect the carrier number of the device and, hence, reduce sensing performance, which could be relieved by sensing film with a certain thickness.[64,65]

Apart from the excellent gas-sensing properties of pristine InSe, 365 nm UV illumination acts as an essential contributor to sensing performance. First, light illumination can refresh the surface of InSe. Normally, in a dark environment, oxygen molecules adsorbed on the edge sites of InSe and the Se defects may not be easily removed, because of low thermal energy. In this case, the number of free electrons is limited and the energy level of surface state is higher than the Fermi level, impeding NO_2 adsorption on InSe. According to the calculation, the bandgap of prepared InSe is 1.44 eV (see Figure S12 in the Supporting Information). Thanks to the narrow and direct bandgap, electron−hole pairs can be easily generated under 365 nm UV illumination, and the preadsorbed oxygen can be desorbed by reacting with the photoexcited holes (eq 4). As a result, the surface state returns to the initial position (below the Fermi level) and thus more active sites are refreshed to adsorb NO_2.[66] Especially in an exhaled gas test, a large number of preadsorbed water and VOCs are also activated under 365-nm UV illumination. Therefore, NO_2 can easily adsorb on the active sites, because of the high binding energy, and increase the resistance with the assistance of water derivatives (see eqs 14 and 15). This could explain the good sensitivity to NO_2 in breath samples. Apart from that, light irradiation can produce sufficient photoexcited electrons. Accordingly, more NO_2 can be adsorbed and capture electrons from the conduction band, and thus the Schottky barriers are elevated (see Figures 6c and 6d),[67,68] which could greatly increase the resistance. Ultimately, the recovery time in NO_2 detection was obviously reduced under 365-nm UV illumination, because photoexcited holes can react with the adsorbed NO_2^- and accelerate the desorption rate. The related reaction is shown as follows:

$$NO_{2^-(ads)} + h^+ \leftrightarrow NO_{2(gas)} \quad (19)$$

In addition to the help from photoexcited holes, photoexcited plasmons in InSe might be another promoting factor for NO_2 desorption.[41] According to the reports, the molecular desorption efficiency is inversely proportional to the excitation wavelength of light. Compared to the wavelength of visible light, 365 nm is more favorable for NO_2 desorption.[69] The comparison of using visible light and UV light is displayed in Figures S13 and S14 in the Supporting Information.

CONCLUSION

This work has described an optoelectronic gas sensor based on direct-bandgap InSe nanosheets prepared via the LPE method. Theoretical results proved that InSe has excellent sensitivity and selectivity to NO_2. Thanks to the outstanding photosensitivity and the superior gas-sensing property of InSe, the

https://dx.doi.org/10.1021/acs.analchem.0c01941
Anal. Chem. 2020, 92, 11277−11287

sensor showed a reversible and extremely high response to ppb-level NO_2 gas under UV illumination. During the tests, UV irradiation can refresh active sites of InSe and promote the adsorption and desorption of NO_2 molecules. As a result, the prepared sensor exhibits good gas-sensing performance, even facing a complexed sample such as human breath. Compared with one-chip InSe devices, the sensors stacked by InSe nanosheets are not only easier to prepare, but also have better long-term stability. It can be considered that light-activated platform based on InSe is a very promising candidate for practical applications in detecting trace NO_2.

■ ASSOCIATED CONTENT

Supporting Information

The Supporting Information is available free of charge at https://pubs.acs.org/doi/10.1021/acs.analchem.0c01941.

Methods of NO_2 detection in human breath and theoretical calculation, the schematic diagram of the gas-sensing measurement system, more details of characterization and sensing performance of InSe/IDEs and one-chip InSe device and the details of O_2 plasma treatment for InSe/IDEs (PDF)

■ AUTHOR INFORMATION

Corresponding Authors

Jia Zhou − *School of Science, Harbin Institute of Technology, Shenzhen 518055, China;* orcid.org/0000-0001-5418-5141; Email: jiazhou@hit.edu.cn

Han Zhang − *Collaborative Innovation Center for Optoelectronic Science & Technology, International Collaborative Laboratory of 2D Materials for Optoelectronics Science and Technology of Ministry of Education, College of Optoelectronic Engineering, Shenzhen University, Shenzhen 518060, China;* orcid.org/0000-0002-2197-7270; Email: hzhang@szu.edu.cn

Yingchun Li − *School of Science, Harbin Institute of Technology, Shenzhen 518055, China;* orcid.org/0000-0002-5371-3587; Email: liyingchun@hit.edu.cn

Authors

Lu Zhang − *School of Science, Harbin Institute of Technology, Shenzhen 518055, China*

Zhongjun Li − *Collaborative Innovation Center for Optoelectronic Science & Technology, International Collaborative Laboratory of 2D Materials for Optoelectronics Science and Technology of Ministry of Education, College of Optoelectronic Engineering, Shenzhen University, Shenzhen 518060, China*

Jiang Liu − *School of Science, Harbin Institute of Technology, Shenzhen 518055, China*

Zhengchun Peng − *Collaborative Innovation Center for Optoelectronic Science & Technology, International Collaborative Laboratory of 2D Materials for Optoelectronics Science and Technology of Ministry of Education, College of Optoelectronic Engineering, Shenzhen University, Shenzhen 518060, China;* orcid.org/0000-0002-7114-1797

Complete contact information is available at: https://pubs.acs.org/10.1021/acs.analchem.0c01941

Author Contributions

$^{\nabla}$These authors contributed equally.

Notes

The authors declare no competing financial interest.

■ ACKNOWLEDGMENTS

The work financially supported by Innovation and Entrepreneurship Projects for Overseas High-Level Talents of Shenzhen (Nos. KQJSCX20180328165437711 and KQTD20170810105439418), National Natural Science Foundation of China (Nos. 81973280 and 81773680). Computer time that was made available by the National Supercomputing Center of China in Shenzhen (Shenzhen Cloud Computing Center) is gratefully acknowledged.

■ REFERENCES

(1) Guarnieri, M.; Balmes, J. R. *Lancet* **2014**, *383*, 1581−1592.
(2) Alving, K.; Weitzberg, E.; Lundberg, J. *Eur. Respir. J.* **1993**, *6*, 1368−1370.
(3) Schwela, D. *Rev. Environ. Health* **2000**, *15*, 13−42.
(4) Barnes, P. J.; Dweik, R. A.; Gelb, A. F.; Gibson, P. G.; George, S. C.; Grasemann, H.; Pavord, I. D.; Ratjen, F.; Silkoff, P. E.; Taylor, D. R.; Zamel, N. *Chest* **2010**, *138*, 682−692.
(5) Broza, Y. Y.; Vishinkin, R.; Barash, O.; Nakhleh, M. K.; Haick, H. *Chem. Soc. Rev.* **2018**, *47*, 4781−4859.
(6) Yao, M. S.; Xiu, J. W.; Huang, Q. Q.; Li, W. H.; Wu, W. W.; Wu, A. Q.; Cao, L. A.; Deng, W. H.; Wang, G. E.; Xu, G. *Angew. Chem., Int. Ed.* **2019**, *58*, 14915−14919.
(7) Campbell, M. G.; Sheberla, D.; Liu, S. F.; Swager, T. M.; Dincă, M. *Angew. Chem., Int. Ed.* **2015**, *54*, 4349−4352.
(8) Campbell, M. G.; Liu, S. F.; Swager, T. M.; Dincă, M. *J. Am. Chem. Soc.* **2015**, *137*, 13780−13783.
(9) Liu, X.; Ma, T.; Pinna, N.; Zhang, J. *Adv. Funct. Mater.* **2017**, *27*, 1702168.
(10) Zhang, L.; Khan, K.; Zou, J.; Zhang, H.; Li, Y. *Adv. Mater. Interfaces* **2019**, *6*, 1901329.
(11) Kumar, R.; Zheng, W.; Liu, X.; Zhang, J.; Kumar, M. *Adv. Mater. Technol.* **2020**, *5*, 1901062.
(12) Xu, T.; Liu, Y.; Pei, Y.; Chen, Y.; Jiang, Z.; Shi, Z.; Xu, J.; Wu, D.; Tian, Y.; Li, X. *Sens. Actuators, B* **2018**, *259*, 789−796.
(13) Kim, Y.-H.; Phan, D.-T.; Ahn, S.; Nam, K.-H.; Park, C.-M.; Jeon, K.-J. *Sens. Actuators, B* **2018**, *255*, 616−621.
(14) Zhou, Y.; Zou, C.; Lin, X.; Guo, Y. *Appl. Phys. Lett.* **2018**, *113*, 082103.
(15) Pham, T.; Li, G.; Bekyarova, E.; Itkis, M. E.; Mulchandani, A. *ACS Nano* **2019**, *13*, 3196−3205.
(16) Espid, E.; Taghipour, F. *Crit. Rev. Solid State Mater. Sci.* **2017**, *42*, 416−432.
(17) Chen, Y.-Z.; Wang, S.-W.; Yang, C.-C.; Chung, C.-H.; Wang, Y.-C.; Chen, S.-W. H.; Chen, C.-W.; Su, T.-Y.; Lin, H.-N.; Kuo, H.-C.; Chueh, Y.-L. *Nanoscale* **2019**, *11*, 10410−10419.
(18) Li, M.; Yang, F. S.; Hsiao, Y. C.; Lin, C. Y.; Wu, H. M.; Yang, S. H.; Li, H. R.; Lien, C. H.; Ho, C. H.; Liu, H. J.; et al. *Adv. Funct. Mater.* **2019**, *29*, 1809119.
(19) Yang, Z.; Jie, W.; Mak, C.-H.; Lin, S.; Lin, H.; Yang, X.; Yan, F.; Lau, S. P.; Hao, J. *ACS Nano* **2017**, *11*, 4225−4236.
(20) Feng, W.; Zheng, W.; Cao, W.; Hu, P. *Adv. Mater.* **2014**, *26*, 6587−6593.
(21) Bandurin, D. A.; Tyurnina, A. V.; Yu, G. L.; Mishchenko, A.; Zólyomi, V.; Morozov, S. V.; Kumar, R. K.; Gorbachev, R. V.; Kudrynskyi, Z. R.; Pezzini, S.; et al. *Nat. Nanotechnol.* **2017**, *12*, 223.
(22) Feng, W.; Wu, J.-B.; Li, X.; Zheng, W.; Zhou, X.; Xiao, K.; Cao, W.; Yang, B.; Idrobo, J.-C.; Basile, L. *J. Mater. Chem. C* **2015**, *3*, 7022−7028.
(23) Cai, Y.; Zhang, G.; Zhang, Y.-W. *J. Phys. Chem. C* **2017**, *121*, 10182−10193.
(24) Ma, D.; Ju, W.; Tang, Y.; Chen, Y. *Appl. Surf. Sci.* **2017**, *426*, 244−252.

(25) Hamer, M. J.; Zultak, J.; Tyurnina, A. V.; Zólyomi, V.; Terry, D.; Barinov, A.; Garner, A.; Donoghue, J.; Rooney, A. P.; Kandyba, V.; et al. *ACS Nano* **2019**, *13*, 2136−2142.
(26) Li, Z.; Qiao, H.; Guo, Z.; Ren, X.; Huang, Z.; Qi, X.; Dhanabalan, S. C.; Ponraj, J. S.; Zhang, D.; Li, J.; et al. *Adv. Funct. Mater.* **2018**, *28*, 1705237.
(27) Curreli, N.; Serri, M.; Spirito, D.; Lago, E.; Petroni, E.; Martín-García, B.; Politano, A.; Gürbulak, B.; Duman, S.; Krahne, R.; et al. *Adv. Funct. Mater.* **2020**, *30*, 1908427.
(28) Yu, Y.; Hu, S.; Su, L.; Huang, L.; Liu, Y.; Jin, Z.; Purezky, A. A.; Geohegan, D. B.; Kim, K. W.; Zhang, Y.; Cao, L. *Nano Lett.* **2015**, *15*, 486−491.
(29) Zhang, S.; Nguyen, T. H.; Zhang, W.; Park, Y.; Yang, W. *Appl. Phys. Lett.* **2017**, *111*, 161603.
(30) Lei, S.; Wen, F.; Ge, L.; Najmaei, S.; George, A.; Gong, Y.; Gao, W.; Jin, Z.; Li, B.; Lou, J.; et al. *Nano Lett.* **2015**, *15*, 3048−3055.
(31) Lei, S.; Ge, L.; Najmaei, S.; George, A.; Kappera, R.; Lou, J.; Chhowalla, M.; Yamaguchi, H.; Gupta, G.; Vajtai, R.; et al. *ACS Nano* **2014**, *8*, 1263−1272.
(32) Kumar, R.; Jenjeti, R. N.; Austeria, M. P.; Sampath, S. *J. Mater. Chem. C* **2019**, *7*, 324−329.
(33) Eshet, H.; Baer, R.; Neuhauser, D.; Rabani, E. *Nat. Commun.* **2016**, *7*, 13178.
(34) Fan, C.; Li, Y.; Lu, F.; Deng, H.-X.; Wei, Z.; Li, J. *RSC Adv.* **2016**, *6*, 422−427.
(35) Hu, P.; Wen, Z.; Wang, L.; Tan, P.; Xiao, K. *ACS Nano* **2012**, *6*, 5988−5994.
(36) Kumar, R.; Goel, N.; Kumar, M. *ACS Sens.* **2017**, *2*, 1744−1752.
(37) Liu, B.; Chen, L.; Liu, G.; Abbas, A. N.; Fathi, M.; Zhou, C. *ACS Nano* **2014**, *8*, 5304−5314.
(38) Sun, J.; Sun, L.; Han, N.; Pan, J.; Liu, W.; Bai, S.; Feng, Y.; Luo, R.; Li, D.; Chen, A. *Sens. Actuators, B* **2019**, *285*, 68−75.
(39) Dang, V. T.; Nguyen, T. T. O.; Truong, T. H.; Le, A. T.; Nguyen, T. D. *Mater. Today Commun.* **2020**, *22*, 100826.
(40) Vijjapu, M. T.; Surya, S. G.; Yuvaraja, S.; Zhang, X.; Alshareef, H. N.; Salama, K. N. *ACS Sens.* **2020**, *5*, 984−993.
(41) Wu, E.; Xie, Y.; Yuan, B.; Zhang, H.; Hu, X.; Liu, J.; Zhang, D. *ACS Sens.* **2018**, *3*, 1719−1726.
(42) Kim, Y. H.; Kim, S. J.; Kim, Y.-J.; Shim, Y.-S.; Kim, S. Y.; Hong, B. H.; Jang, H. W. *ACS Nano* **2015**, *9*, 10453−10460.
(43) Ou, J. Z.; Ge, W.; Carey, B.; Daeneke, T.; Rotbart, A.; Shan, W.; Wang, Y.; Fu, Z.; Chrimes, A. F.; Wlodarski, W.; et al. *ACS Nano* **2015**, *9*, 10313−10323.
(44) Yim, C.; Lee, K.; McEvoy, N.; O'Brien, M.; Riazimehr, S.; Berner, N. C.; Cullen, C. P.; Kotakoski, J.; Meyer, J. C.; Lemme, M. C.; Duesberg, G. S. *ACS Nano* **2016**, *10*, 9550−9558.
(45) Kumar, R.; Jenjeti, R. N.; Sampath, S. *ACS Sens.* **2020**, *5*, 404−411.
(46) Kim, Y.; Kwon, K. C.; Kang, S.; Kim, C.; Kim, T. H.; Hong, S.-P.; Park, S. Y.; Suh, J. M.; Choi, M.-J.; Han, S.; Jang, H. W. *ACS Sens.* **2019**, *4*, 2395−2402.
(47) Jannat, A.; Haque, F.; Xu, K.; Zhou, C.; Zhang, B. Y.; Syed, N.; Mohiuddin, M.; Messalea, K. A.; Li, X.; Gras, S. L.; et al. *ACS Appl. Mater. Interfaces* **2019**, *11*, 42462−42468.
(48) Huang, Y.; Jiao, W.; Chu, Z.; Ding, G.; Yan, M.; Zhong, X.; Wang, R. *J. Mater. Chem. C* **2019**, *7*, 8616−8625.
(49) Ray, S. *Sens. Actuators, B* **2016**, *222*, 492−498.
(50) Barsan, N.; Weimar, U. *J. Electroceram.* **2001**, *7*, 143−167.
(51) Kumar, R.; Al-Dossary, O.; Kumar, G.; Umar, A. *Nano-Micro Lett.* **2015**, *7*, 97−120.
(52) Liu, D.; Tang, Z.; Zhang, Z. *Sens. Actuators, B* **2020**, *303*, 127114.
(53) Song, Y. G.; Shim, Y.-S.; Suh, J. M.; Noh, M.-S.; Kim, G. S.; Choi, K. S.; Jeong, B.; Kim, S.; Jang, H. W.; Ju, B.-K.; Kang, C.-Y. *Small* **2019**, *15*, 1902065.
(54) Hsu, C.-L.; Chang, L.-F.; Hsueh, T.-J. *Sens. Actuators, B* **2017**, *249*, 265−277.
(55) Tan, Y.; Yu, K.; Yang, T.; Zhang, Q.; Cong, W.; Yin, H.; Zhang, Z.; Chen, Y.; Zhu, Z. *J. Mater. Chem. C* **2014**, *2*, 5422−5430.
(56) Yan, W.; Worsley, M. A.; Pham, T.; Zettl, A.; Carraro, C.; Maboudian, R. *Appl. Surf. Sci.* **2018**, *450*, 372−379.
(57) Mansour, E.; Vishinkin, R.; Rihet, S.; Saliba, W.; Fish, F.; Sarfati, P.; Haick, H. *Sens. Actuators, B* **2020**, *304*, 127371.
(58) Bag, A.; Lee, N.-E. *J. Mater. Chem. C* **2019**, *7*, 13367−13383.
(59) Hua, Z.; Li, Y.; Zeng, Y.; Wu, Y. *Sens. Actuators, B* **2018**, *255*, 1911−1919.
(60) Leenaerts, O.; Partoens, B.; Peeters, F. *Phys. Rev. B: Condens. Matter Mater. Phys.* **2008**, *77*, 125416.
(61) Yue, Q.; Shao, Z.; Chang, S.; Li, J. *Nanoscale Res. Lett.* **2013**, *8*, 425.
(62) Sakai, G.; Matsunaga, N.; Shimanoe, K.; Yamazoe, N. *Sens. Actuators, B* **2001**, *80*, 125−131.
(63) Zhang, J.; Qin, Z.; Zeng, D.; Xie, C. *Phys. Chem. Chem. Phys.* **2017**, *19*, 6313−6329.
(64) Chen, I.-C.; Holland, S.; Hu, C. *J. Appl. Phys.* **1987**, *61*, 4544−4548.
(65) Chen, H.; Chen, Y.; Zhang, H.; Zhang, D. W.; Zhou, P.; Huang, J. *Adv. Funct. Mater.* **2018**, *28*, 1801035.
(66) Li, G.; Sun, Z.; Zhang, D.; Xu, Q.; Meng, L.; Qin, Y. *ACS Sens.* **2019**, *4*, 1577−1585.
(67) Kathiravan, D.; Huang, B.-R.; Saravanan, A.; Prasannan, A.; Hong, P.-D. *Sens. Actuators, B* **2019**, *279*, 138−147.
(68) Wang, X.; Liu, Y.; Dai, J.; Chen, Q.; Huang, X.; Huang, W. *Chem. - Eur. J.* **2020**, *26*, 3870−3876.
(69) Chen, R. J.; Franklin, N. R.; Kong, J.; Cao, J.; Tombler, T. W.; Zhang, Y.; Dai, H. *Appl. Phys. Lett.* **2001**, *79*, 2258−2260.

https://dx.doi.org/10.1021/acs.analchem.0c01941
Anal. Chem. 2020, 92, 11277−11287